

A FAR-INFRARED CHARACTERIZATION OF 24 μ M SELECTED GALAXIES AT $0 < Z < 2.5$ USING STACKING AT 70 μ M AND 160 μ M IN THE COSMOS FIELD

NICHOLAS LEE¹, EMERIC LE FLOC'H¹, D. B. SANDERS¹, D. T. FRAYER², STEPHANE ARNOUTS³, OLIVIER ILBERT⁴, HERVÉ AUSSÉL⁵, MARA SALVATO^{6,7}, N.Z. SCOVILLE⁶, JEYHAN S. KARTALTEPE⁸

Draft version October 24, 2018

ABSTRACT

We present a study of the average properties of luminous infrared galaxies detected directly at 24 μ m in the COSMOS field using a median stacking analysis at 70 μ m and 160 μ m. Over 35000 sources spanning $0 \leq z \leq 3$ and $0.06 \text{ mJy} \leq S_{24} \leq 3.0 \text{ mJy}$ are stacked, divided into bins of both photometric redshift and 24 μ m flux. We find no correlation of S_{70}/S_{24} flux density ratio with S_{24} , but find that galaxies with higher S_{24} have a lower S_{160}/S_{24} flux density ratio. These observed ratios suggest that 24 μ m selected galaxies have warmer spectral energy distributions (SEDs) at higher mid-IR fluxes, and therefore have a possible higher fraction of active galactic nuclei. Comparisons of the average S_{70}/S_{24} and S_{160}/S_{24} colors with various empirical templates and theoretical models show that the galaxies detected at 24 μ m are consistent with “normal” star-forming galaxies and warm mid-IR galaxies such as Mrk 231, but inconsistent with heavily obscured galaxies such as Arp 220. We perform a χ^2 analysis to determine best fit galactic model SEDs and total IR luminosities for each of our bins. We compare our results to previous methods of estimating L_{IR} and find that previous methods show considerable agreement over the full redshift range, except for the brightest S_{24} sources, where previous methods overpredict the bolometric IR luminosity at high redshift, most likely due to their warmer dust SED. We present a table that can be used as a more accurate and robust method for estimating bolometric infrared luminosity from 24 μ m flux densities.

Subject headings: galaxies: evolution - galaxies: high-redshift - galaxies: statistics - infrared: galaxies

1. INTRODUCTION

Although rare in the present-day universe, luminous infrared galaxies (LIRGs) were much more numerous in the past, and they may have played a significant role in the evolution of a large fraction of $L > L^*$ galaxies (Sanders & Mirabel 1996; Blain et al. 2002; Lagache et al. 2004; Le Floc'h et al. 2005). However, their exact contribution is still poorly understood due to two limitations that have plagued deep surveys performed so far: (1) the difficulty to identify the most obscured and distant of these objects, as well as measure their redshifts (they are often faint at optical wavelengths because of dust extinction, Houck et al. 2005), and (2) the difficulty to accurately characterize their nature (bolometric luminosity, mass, physical processes powering their energy output). Furthermore, because of limited sensitivity of current space- (*Spitzer* MIPS) and ground-based (SCUBA, BOLO-CAM, MAMBO, AzTEC,...) observations in the far-

IR/submillimeter, only a small number of the most luminous of these sources has been studied in detail. In addition, at high redshifts there are significant limitations due to confusion, which results from the very large instrument beam characterizing current far-IR/submillimeter observations.

Many previous studies of LIRGs have been based on data obtained with the *Spitzer Space Telescope*, in particular with the Multiband Imaging Photometer (MIPS, Rieke et al. 2004) at 24 μ m, the detector’s most sensitive band. Using extrapolations based on libraries of galactic infrared (IR) spectral energy distributions (SEDs), the observed 24 μ m flux is converted to a bolometric IR luminosity, $L_{\text{IR}} \equiv L(8\text{--}1000\mu\text{m})$, which is then used to calculate properties such as instantaneous star formation rate (SFR). However, at higher redshifts the 24 μ m band probes shorter rest frame wavelengths, probing rest frame 12 μ m at $z \sim 1$, and rest frame 8 μ m at $z \sim 2$. The typical peak of the IR SED of star-forming galaxies and galaxies containing active galactic nuclei (AGN) falls around 50–200 μ m; at higher redshifts, the 24 μ m band probes wavelengths farther away from the peak of the IR SED and begins to be heavily affected by broad mid-infrared PAH emission and silicate absorption features.

Observations at longer wavelengths, such as in the *Spitzer* MIPS 70 μ m and 160 μ m bands (which probe rest frame 24 μ m and 54 μ m at $z \sim 2$, respectively), are needed to more accurately characterize the bolometric luminosity, especially at higher redshifts. However, the MIPS 70 μ m and 160 μ m bands are significantly less sensitive and have worse angular resolution than the 24 μ m band. This leads to a drastic decrease in the number of

¹ Institute for Astronomy, University of Hawaii, 2680 Woodlawn Dr., Honolulu, HI, 96822, USA

² Infrared Processing and Analysis Center, California Institute of Technology 100-22, Pasadena, CA 91125, USA

³ Canada France Hawaii Telescope Corporation, 65-1238 Mamalahoa Hwy, Kamuela, HI 96743, USA

⁴ Laboratoire d’Astrophysique de Marseille, BP 8, Traverse du Siphon, 13376 Marseille Cedex 12, France

⁵ UMR AIM (CEA-UP7-CNRS), CEA-Saclay, Orme des Merisiers, bât. 709, F-91191 Gif-sur-Yvette Cedex, France

⁶ California Institute of Technology, MS 105-24, 1200 East California Boulevard, Pasadena, CA 91125, USA

⁷ Max Planck Institute for Plasma Physics and Cluster of Excellence, Boltzmann Strasse 2, Garching, D-85748, Germany

⁸ National Optical Astronomy Observatory, 950 North Cherry Avenue, Tucson, AZ, 85719, USA

sources directly detected at 70 μm and 160 μm , and the galaxies that are detected are biased toward the most luminous sources. Therefore, we use a stacking analysis (as in Dole et al. 2006; Papovich et al. 2007) to study the average 70 μm and 160 μm flux densities of galaxies detected at 24 μm . In using a stacking analysis we lose the ability to study individual galaxies, but find average properties of galaxies that would otherwise be undetectable.

In this work we explore the average mid- to far-IR flux densities of galaxies detected at 24 μm and derive a more accurate method to estimate bolometric IR luminosity. To accomplish this, we measure stacked 70 μm and 160 μm flux densities of galaxies detected at 24 μm in the Cosmic Evolution Survey (COSMOS) field, binned in both redshift and 24 μm flux. We use these stacked fluxes to examine the evolution of mid- to far-IR colors of galaxies as a function of luminosity and redshift. Our stacked fluxes are fit to libraries of galactic IR SED templates, from which we derive an estimate of the average bolometric IR luminosity. Papovich et al. (2007) carried out a similar study employing stacking at 70 μm and 160 μm , but their analysis was limited by area, with a significantly smaller number of sources. With an area almost 10 times larger, we obtain more reliable statistics and the ability to bin our sources in narrower bins of redshift and flux. Our stacked fluxes will eventually be merged with Herschel PACS (100 & 160 μm), Herschel SPIRE (200–500 μm), and SCUBA2 data to get the best sampled SEDs of the high- z literature.

Throughout this work we denote flux density, f_ν in MIPS 24 μm , 70 μm , and 160 μm bands as S_{24} , S_{70} , and S_{160} , respectively. When calculating rest-frame quantities, we use a cosmology with $\Omega_m = 0.3$, $\Lambda = 0.7$, and $H_0 = 70 \text{ km s}^{-1} \text{ Mpc}^{-1}$.

2. DATA

We use data from the *Cosmic Evolution Survey* (COSMOS) field (Scoville et al. 2007), a $\sim 2 \text{ deg}^2$ field centered at right ascension $10^{\text{h}}00^{\text{m}}28^{\text{s}}.6$, declination $02^{\circ}12'21''0$ (J2000) with extensive multiwavelength imaging and spectroscopic coverage. In this study, we make use of the COSMOS *Spitzer* (S-COSMOS; Sanders et al. 2007) observations, specifically the data taken by MIPS in the 24 μm , 70 μm , and 160 μm bands.

2.1. 24 μm Catalog

The 24 μm data reduction and source extraction are detailed in Le Floc'h et al. (2009). The 24 μm sources were detected using the automatic procedure of the SExtractor software (Bertin & Arnouts 1996), and the flux densities were measured with multiple iterations of the point-spread function (PSF) fitting technique of the DAOPHOT package (Stetson 1987). Following the convention adopted by the *Spitzer Science Center*, a stellar 10,000 K blackbody spectrum was assumed as the reference SED for the 24 μm flux density measurements. The final source list is complete to more than 90% above a 24 μm flux of $S_{24} \sim 80 \mu\text{Jy}$, and according to simulations, is still reliable down to fluxes as faint as $60 \mu\text{Jy}$, despite a lower completeness of 75%. The source list we use for our stacking analysis includes all sources with $S_{24} \geq 60 \mu\text{Jy}$.

2.2. 70 μm and 160 μm Mosaics

The MIPS 70 μm and 160 μm data were reduced and processed by Frayer et al. (2009). In short, the data were reduced using the Germanium Reprocessing Tools (GeRT, version 20060415) and additional specialized scripts developed for processing survey data from the MIPS-Germanium 70 μm and 160 μm detectors. The final 70 μm and 160 μm mosaics have an image pixel scale of $4''$ and $8''$ and point-source noise (1σ) of 1.7 mJy and 13 mJy, respectively, although there are local background fluctuations across the image depending on the local density of sources. Frayer et al. (2009) find 1512 sources at 70 μm , and 499 sources at 160 μm ($\geq 5.0\sigma$), but these detections represent the most luminous sources. In our stacking analysis, we do not treat these sources differently than 24 μm sources that were not detected at 70 μm and 160 μm (see Section 3).

2.3. Photometric Redshifts

The extensive multiwavelength coverage of the COSMOS field leads to photometric redshifts (hereafter photo- z) with an accuracy better than ever achieved in any other field, as detailed in Ilbert et al. (2009). Optical counterparts of the 24 μm sources were found from correlating the data with the K_s -band COSMOS catalog of McCracken et al. (2010), as detailed in Le Floc'h et al. (2009). Photo- z were then calculated using fluxes in 30 bands, covering the far-UV at 1550 \AA to the mid-IR at 8.0 μm . The uncertainties in the photo- z depend primarily on the redshift and apparent i^+ magnitude of the source, with errors increasing with fainter and more distant galaxies, but a comparison with faint spectroscopic samples in the COSMOS field revealed a dispersion as low as $\sigma_{\Delta z/(1+z_s)} = 0.06$ for sources with $23 \text{ mag} < i_{\text{AB}}^+ < 25 \text{ mag}$ at $1.5 \lesssim z \lesssim 3$ (Lilly et al. 2007).

Approximately 1000 of our 24 μm sources are also detected in the X-ray by *XMM-Newton* (Brusa et al. 2010), and for these sources we use the photo- z 's derived from Salvato et al. (2009), who have the best photometric redshifts ever produced for AGNs. In all, we have reliable photo- z for 35,797 sources detected at 24 μm ($\sim 92\%$ of the 38679 total 24 μm sources). We do not use the remaining sources without photo- z 's in our study, but these sources are generally at the low S_{24} end of our sample, where we have enough sources to perform a meaningful analysis.

3. ANALYSIS

To study the average 70 μm and 160 μm properties of the LIRGs in the COSMOS field, we employ a median stacking analysis to overcome the poor sensitivity of the 70 μm and 160 μm MIPS detectors. Stacking of IR emission has proven valuable for studies such as average 24 μm fluxes in faint galaxies (Zheng et al. 2006) and contributions to the far IR extragalactic background (Dye et al. 2007). A stacking analysis of 70 μm and 160 μm fluxes of galaxies selected at 24 μm has been performed by Papovich et al. (2007). However, their analysis used data taken in the Extended *Chandra* Deep Field (ECDF-S), which covers 775 arcmin^2 , and includes only 395 sources. As a result, they do not have significant detections in some of their lower 24 μm flux bins. With the COSMOS data, we have almost 100 times as many sources (stacking efficiency goes as $\sim N^{\frac{1}{2}}$), and will be

able to make a much more detailed analysis with narrower bins in both redshift and rest-frame mid-IR luminosity.

We divide our 24 μm source list into bins of both redshift and S_{24} before stacking. Redshift bins ensure that the fluxes we stack were emitted at the same rest-frame wavelength so that we probe the same parts of the SED, and S_{24} bins separate galaxies with different IR luminosities. Our redshift and S_{24} bins were chosen to maximize the number of sources in each bin while providing the best coverage in redshift and flux; Table 1 lists the bin limits and the corresponding number of sources in each bin.

3.1. Stacking Methodology

We begin by taking a 40×40 pixel ($2.7' \times 2.7'$ at 70 μm and $5.3' \times 5.3'$ at 160 μm) cutout centered around each 24 μm source in a given bin. For reference, the FWHM of the 70 μm mosaic is $18.6''$ and the FWHM of the 160 μm mosaic is $39''$. The size of the cutout does not affect the measured average (stacked) flux as long as the cutout encompasses a large enough area to make a local background estimate. We center each 70 μm and 160 μm subimage on the astrometric coordinates of the 24 μm source using a bilinear cubic interpolation, and then subtract a local background from each subimage; the local background is calculated from pixels exterior to $\sim 1'$ and $\sim 2'$ at 70 μm and 160 μm , respectively. Before creating our stacked image, we rotate each subimage by 90° with respect to the previous subimage to reduce the effects of image artifacts in our analysis.

We then “stack” these subimages, aligned at the center (on-source) position and calculate a median flux density at each pixel position. A median stacking analysis is preferable to mean stacking because the median analysis is more stable and robust to small numbers of bright sources. The main problem with a mean stacking analysis is that it is very sensitive to bright outliers, which contaminate on-source flux measurements and introduce considerable noise from nearby, bright neighbors. Most mean stacking studies avoid this problem by removing bright sources from all images before stacking, but this technique solves one problem and creates two more. Removing bright sources introduces a slight bias against more luminous sources and the resultant stacked flux varies based on the exact flux density cutoff chosen; someone who chooses to remove all sources $\geq 4\sigma$ will measure a different flux than someone who chooses to remove all sources $\geq 3\sigma$. The median stacking analysis avoids these problems, but is more difficult to interpret. From detailed comparisons of median and mean stacking, White et al. (2007) find that in “a limit where almost all the values in our sample are small compared with the noise . . . it is straightforward to interpret our median stack measurements as representative of the mean for the population of sources.” Our sample fits this description, with only $\sim 4\%$ of our sources detected at 70 μm , and less than 2% of our sources detected at 160 μm , so we take the results of our median analysis as representative of the mean flux density.

We calculate the flux of our final stacked image using the DAOPHOT-type photometry IDL procedure, APER, with photometry aperture of $35''$ and sky annulus radii of $39''$ – $65''$ at 70 μm (at 160 μm , we use an aperture of

$48''$ and sky radii of $64''$ – $128''$). We use these radii in conjunction with the published MIPS aperture corrections for a 10 K blackbody given by the Spitzer Science Center (1.48 at 70 μm and 1.642 at 160 μm) to estimate the total flux density from our stacked source.

3.2. Uncertainties in Stacking

We measure an error in our stacked flux densities from the variance in the local background of the stacked image and the uncertainty in the mean sky brightness. The absolute calibration of the MIPS detector at long wavelengths is $\sim 10\%$ (Gordon et al. 2007; Stansberry et al. 2007), and this dominates the errors in our stacked images in all but the noisiest of bins. Since a median analysis is a ranking measurement, we find an error in the median by sorting each pixel and then measuring the difference between the middle (median) value and the value that is $N^{1/2}$ ranks away from the middle, where $N^{1/2}$ is the Poissonian noise from a bin with N sources. For all bins, this represents an almost negligible source of error.

To test for confusion from nearby bright sources, we searched the 24 μm catalog for nearby sources that would fall within the apertures used to measure the 70 μm and 160 μm flux densities. We find that only $\sim 3\%$ of our sources have a neighbor within the (larger) aperture used to measure the 160 μm flux. However, the location of each of these nearby neighbors relative to the target source will not be uniform, which suggests that the contribution of nearby neighbors detected at 24 μm to our final stacked flux should be negligible. The fraction of galaxies with neighbors within the 160 μm aperture is fairly constant in all bins.

Confusion from faint sources can also add uncertainty to flux measurements; galaxy clustering suggests that the confusion from faint sources will generally be more significant near detected sources than at off-source background positions. The proper method to account for confusion from faint sources is still currently debated, but the uncertainty is expected to be important mostly for data at very long wavelengths, such as in the submillimeter regime, which is generally confusion-limited (H. Dole 2010, private communication). The COSMOS MIPS data used in our stacking analysis are not confusion-limited, so we expect a negligible contribution from confusion.

4. RESULTS

4.1. Average 70 μm and 160 μm Flux Densities

We performed a median stacking analysis for all 56 bins of redshift and S_{24} in our sample at both 70 μm and 160 μm . From a visual inspection of the images produced by the stacking analysis, we find clean detections in 88% of our 70 μm stacks, and 73% of our 160 μm stacks. The rest of the stacks can be split into two categories: (1) non-detections, which have no signal at all, and (2) bad detections, which have a visible, but distorted signal that does not resemble a clean PSF. The non-detections do not have enough signal to noise for an average source to emerge, but the bad detections do not always have this same problem. The non-detections and bad detections are mostly in low flux and high redshift bins, although there are a few bad detections in the low-

est flux bins with low/intermediate redshifts. The bins containing the non-detections and bad detections all have a fairly high number of sources, so we believe the lack of a clean detection is due simply to the faintness of the sources we are trying to stack. In the rest of our analysis, we treat the non-detections as upper limits, but include the bad detections in our full analysis. Tables 2 and 3 list the measured 70 μm and 160 μm fluxes and errors in each of our bins, with upper limits given for non-detections. Figure 1 displays an example of a clean detection and a bad detection at 70 μm .

4.2. Evolution of 70/24 μm and 160/24 μm Color with 24 μm Flux

The mid- to far-infrared flux density ratios (or colors) of our stacked galaxies give us insight into the properties of the dust emission from these galaxies. Figure 2 shows the average stacked S_{70}/S_{24} and S_{160}/S_{24} flux ratios of our sources, with each color representing a different redshift bin. From the top panel of Figure 2, we see that the average S_{70}/S_{24} colors fall in the range $3 \lesssim S_{70}/S_{24} \lesssim 20$, which is roughly consistent with results reported in Papovich et al. (2007), who found an average $S_{70}/S_{24} \approx 9$. They also find that sources with $S_{24} > 250 \mu\text{Jy}$ have a lower average flux ratio ($S_{70}/S_{24} \approx 5$), but we do not see a trend of decreasing S_{70}/S_{24} flux ratio with increasing S_{24} . Our results show a mostly flat S_{70}/S_{24} color with respect to S_{24} .

We also find a trend of decreasing S_{70}/S_{24} flux ratio with increasing redshift (from $S_{70}/S_{24} \approx 15$ at $z \sim 0.3$ to $S_{70}/S_{24} \approx 5$ at $z \sim 2$). This does not necessarily mean that high redshift galaxies have lower S_{70}/S_{24} flux ratios because at higher redshifts, the observed S_{70}/S_{24} measures flux ratios at shorter rest-frame wavelengths. Galaxies with strong mid-IR polycyclic aromatic hydrocarbon (PAH) features have mid-IR ($\sim 24 \mu\text{m}$) emission that is flatter than their far-IR ($\sim 70 \mu\text{m}$) emission, which will lead to a lower observed S_{70}/S_{24} flux ratio at higher redshifts, even when observing galaxies with identical SEDs. We explore the dependence of S_{70}/S_{24} on redshift further in Section 5.1 through comparisons of our stacking results with models.

Although we do not see a strong trend in S_{70}/S_{24} ratio with S_{24} , we see a clear trend of decreasing S_{160}/S_{24} ratio with increasing S_{24} in the bottom panel of Figure 2. The average S_{160}/S_{24} ratios we measure range from $10 \lesssim S_{160}/S_{24} \lesssim 100$ and are much larger than the S_{70}/S_{24} ratios because the 160 μm band samples fluxes emitted at wavelengths closer to the peak of galactic IR SEDs. Papovich et al. (2007) did not have high enough signal-to-noise in their stacks at 160 μm to explore S_{160}/S_{24} ratios, but they find average S_{160} ranging from 3.8 to 10.5 mJy, broadly consistent with our values of S_{160} in the lower S_{24} bins.

Figure 2 shows that the brightest 24 μm sources have low S_{160}/S_{24} ratios. Given that S_{24} broadly correlates with IR luminosity, this means that on average, galaxies with brighter IR luminosities have lower S_{160}/S_{24} flux ratios, and therefore flatter spectra. This trend is true in all our redshift bins, although the effect is less pronounced in our highest redshift bins.

The warmer S_{160}/S_{24} colors in the higher S_{24} bins suggest that these sources, on average, have a higher fraction of AGNs (Sanders & Mirabel 1996; Laurent et al. 2000).

Dust grains in the dusty torus around AGN can be heated up to their sublimation temperature (1500 - 2000 K), while dust grains in the diffuse interstellar medium and star-forming regions of galaxies are stochastically heated to lower temperatures around $30 \sim 40$ K, or up to 200-400 K in HII regions. The emission from the warmer dust grains around AGN will mostly dominate in the mid-IR wavelengths, while the emission from the colder grains in star-forming regions will dominate the far-IR. Thus, galaxies powered by AGN will be flatter in their mid-IR to far-IR colors.

It should be noted that although we do find a trend of flatter S_{160}/S_{24} ratios that is indicative of a higher fraction of AGN, our sources are still most likely dominated by star formation at the $\sim 85\%$ – 90% level (Le Floc’h et al. 2009). Out of our over 35000 sources, only ~ 1000 have X-ray counterparts, suggesting that AGN make up a negligible population of our bins, except for possibly the highest S_{24} bins. Figure 3 displays the fraction of sources in each bin that are also detected in the X-ray by *XMM-Newton*. At dim S_{24} bins, we see that *XMM-Newton* sources indeed account for a low percentage of our sources. At bright S_{24} bins, the X-ray-detected sources begin to account for an appreciable fraction of our sources, but this does not mean that the mid- and far-IR fluxes of these sources are dominated by AGN. We discuss this further in Section 5.2.

5. DISCUSSION

5.1. Comparison to Models

In this section, we compare the results of our stacking analysis with the expected fluxes and colors from theoretical models and empirical templates. We first compare our stacked S_{70}/S_{24} and S_{160}/S_{24} flux ratios with empirical models of “normal” star forming galaxies by Dale & Helou (2002, hereafter DALE) and models of Arp 220 and Mrk 231 from the SWIRE template library (Polletta et al. 2007). We then constrain the average IR luminosity for each bin by fitting to many libraries of theoretical models and empirical templates.

Figure 4 plots S_{70}/S_{24} and S_{160}/S_{24} color as a function of redshift, along with the expected values from the DALE models of star forming galaxies and the SWIRE models of Arp 220 and Mrk 231. The DALE models are a one parameter family of models and we show models that cover a range of $1 < \alpha < 2.5$, which describe normal star-forming galaxies with $8.3 < \log(L_{\text{IR}}) < 14.3$. Arp 220 is a well-studied galaxy representative of heavily obscured ULIRGs, while Mrk 231 is representative of galaxies with warm mid-IR colors which are known to host AGN. We use the code *Le Phare*⁹ developed by S. Arnouts and O. Ilbert to determine the flux ratios of the DALE and SWIRE models at varying redshifts. *Le Phare* is a data analysis package used primarily to compute photometric redshifts, but a preliminary phase of the code also computes theoretical magnitudes, given SED libraries and filter bands. We can see immediately that the average colors determined from our stacking analysis fall within the region spanned by normal star-forming galaxies and Mrk 231, but our colors do not match those of Arp 220 at any redshift. This suggests that our 24 μm selection is biased against heavily obscured objects like Arp 220.

⁹ <http://www.cfht.hawaii.edu/~arnouts/lephare.html>

5.2. Best-fit Model SEDs and Average Total IR Luminosity

We use *Le Phare* to perform a χ^2 analysis to find best-fit galactic model SEDs for the stacked fluxes calculated in each bin. We use the empirical templates of Dale & Helou (2002), Lagache et al. (2003), Chary & Elbaz (2001), and the theoretical radiation pressure models of Siebenmorgen & Krügel (2007), finding the SED from each library that best fit our stacked data at the correct redshift. The average S_{24} , S_{70} , and S_{160} in each bin are plotted along with the best fit models in Figures 5a–5h, arranged by redshift (Figures 5b–5h are only available in the online version of the paper). Fluxes from the “non-detected” bins are shown as upper limits. The parameter space spanned by all four of the models is shaded to give an idea of the spread of possible SEDs that fit the data.

For our model fits, we use four different libraries of “normal” star-forming galaxies. We do have a small fraction of *XMM-Newton*-detected sources that contain AGN, especially in the highest flux bins, but this does not imply that the mid-IR and/or far-IR fluxes of these galaxies is dominated by the AGN itself (many X-ray sources are PAH dominated in the infrared). Because of the small number of sources, we are unable to perform a separate stacking analysis of only these X-ray sources. Although we cannot account for the true contribution of AGN contamination, the tight fits we see suggest that most of our sources are indeed star formation dominated.

From the maximum likelihood function of the χ^2 analysis, we estimate a median L_{IR} and 1σ uncertainties in each bin of our stacking analysis. We repeat this measurement for each library separately, and then take the mean of the four L_{IR} values to estimate the true luminosity. The dispersion of the luminosities derived from the different libraries is $\sim 6\%(3\sigma)$ in all our bins, which suggests that the four libraries are fairly consistent in their estimates of the best-fit L_{IR} . We add the 1σ uncertainties from each library in quadrature to estimate the error in L_{IR} , and find typical 3σ errors around 3%. The average IR luminosities and errors measured for each of our bins are listed in Table 4. Bins classified as non-detections at both $70\ \mu\text{m}$ and $160\ \mu\text{m}$ are marked as upper limits. As expected, we see that total IR luminosity increases with S_{24} and with redshift. These galaxies span a large range of IR luminosity, covering “normal” galaxies ($L_{\text{IR}} \leq 10^{11} L_{\odot}$), LIRGs ($10^{11} L_{\odot} \leq L_{\text{IR}} \leq 10^{12} L_{\odot}$), and ultra luminous infrared galaxies (ULIRGs; $L_{\text{IR}} \geq 10^{12} L_{\odot}$). To test our uncertainties, we also found best fit SEDs using $70\ \mu\text{m}$ and $160\ \mu\text{m}$ flux densities that were offset by the errors given in Tables 2 and 3 and then measured L_{IR} from these fits. We find discrepancies much less than 6% from this trial, suggesting that our derived infrared luminosities are robust within the errors in our stacking analysis.

Table 4 gives a relation between *observed* S_{24} and total IR luminosity, with no need for a k -correction. This is an extremely valuable tool given the poor sensitivity of longer wavelength instruments, and provides an effective way to estimate L_{IR} when only having $24\ \mu\text{m}$ data. Some caution must be taken when using Table 4 to estimate L_{IR} . Although the agreement between the best-fit models from many libraries is fairly robust, it is not a

complete description of the errors. For most of these bins, we do not have data on the Rayleigh Jean side of our IR SEDs, which means we cannot estimate the cold dust component and its contribution to L_{IR} . This means that Table 4 is valid under assumption that the libraries used are representative of the diversity of the SEDs beyond $160\ \mu\text{m}/(1+z)$. These results will be tested in the near future with Herschel and SCUBA2.

Figure 6 shows a comparison of L_{IR} calculated from our stacking analysis and L_{IR} calculated from extrapolating mid-IR fluxes from only S_{24} based on the Dale SED libraries, as is common practice. In general, the two methods are in good agreement at low redshifts, but the L_{IR} calculated using only $24\ \mu\text{m}$ data is an overestimate of the true L_{IR} at high redshifts, especially for the brighter S_{24} sources. This is most likely due to the warmer dust SEDs that we find in the bright S_{24} sources (Section 4.2). Our results are consistent with the findings of Calzetti et al. (2007), who find that rest-frame $24\ \mu\text{m}$ flux is a much better indicator of bolometric infrared luminosity than $8\ \mu\text{m}$ flux, and with the findings of Papovich et al. (2007), who find that the L_{IR} estimated without taking into account stacked $70\ \mu\text{m}$ and $160\ \mu\text{m}$ fluxes overestimates the true L_{IR} . To summarize, extrapolating a bolometric infrared luminosity from a $24\ \mu\text{m}$ flux density without taking into account $70\ \mu\text{m}$ and $160\ \mu\text{m}$ flux will result in an overestimate of L_{IR} at high redshifts. Table 4 will give a more accurate and robust estimate of L_{IR} at these redshifts.

6. SUMMARY

We perform a median stacking analysis on over 35000 sources detected directly at $24\ \mu\text{m}$ in the COSMOS field at $0 \leq z \leq 3$ and $0.06\ \text{mJy} \leq S_{24} \leq 3.0\ \text{mJy}$ to study their average flux densities at $70\ \mu\text{m}$ and $160\ \mu\text{m}$. Of the 56 bins used, 95% had detections at $70\ \mu\text{m}$ and 93% had detections at $160\ \mu\text{m}$. Analysis of the S_{70}/S_{24} and S_{160}/S_{24} flux density ratios suggest the following.

- $24\ \mu\text{m}$ sources have average flux-density ratios consistent with empirical models of “normal” star-forming galaxies or with warm mid IR galaxies, like Mrk 231, which are known to host AGN.
- $24\ \mu\text{m}$ sources have average flux-density ratios that are inconsistent with Arp 220, which suggests that $24\ \mu\text{m}$ is not very useful for finding heavily obscured objects like Arp 220.
- Sources with brighter S_{24} have warmer S_{160}/S_{24} flux ratios, decreasing by a factor of 2 from $0.1 \lesssim S_{24}/\text{mJy} \lesssim 1.0$, which implies that galaxies with brighter infrared luminosities have a higher fraction of AGN.

Our stacking analysis provides the largest statistical study of the average far-IR flux densities of the faint $24\ \mu\text{m}$ population. A comparison of the average far-IR fluxes to libraries of empirical templates and theoretical models allows us to estimate the total IR luminosity of a typical galaxy detected at $24\ \mu\text{m}$ within certain redshift and S_{24} bins. We find that previous studies based on extrapolating L_{IR} from $24\ \mu\text{m}$ data, without far-IR stacking, generally overpredict the total infrared luminosity, especially at higher redshifts. A more accurate method

for estimating L_{IR} using only $24\ \mu\text{m}$ flux and redshift is provided in Table 4, which takes into account the average mid- and far-IR fluxes of $24\ \mu\text{m}$ selected galaxies.

It is a pleasure to acknowledge the contribution from all our colleagues of the COSMOS collaboration. More information on the COSMOS survey is available at <http://www.astro.caltech.edu/cosmos>. This work is based on observations made with the *Spitzer Space Telescope*, a facility operated by NASA/JPL. Financial supports were provided by NASA through contracts 1289085, 1310136, 1282612, and 1298231 issued by the Jet Propulsion Laboratory. We are grateful to Herve Dole for insightful discussions on stacking techniques.

TABLE 1
NUMBER OF SOURCES IN EACH REDSHIFT AND S_{24} BIN

S_{24} (mJy)	Redshift Range							
	0–0.4	0.4–0.6	0.6–0.8	0.8–1.0	1.0–1.2	1.2–1.6	1.6–2	2–3
0.06–0.08	724	578	923	1281	1025	1573	1006	1002
0.08–0.10	501	423	701	887	688	1045	749	684
0.10–0.15	841	681	1011	1479	1092	1395	1280	896
0.15–0.20	528	421	588	834	535	557	629	482
0.20–0.50	1152	745	930	1354	628	597	790	604
0.50–1.00	408	153	136	187	61	75	73	78
1.00–3.00	228	35	28	26	11	21	20	21

TABLE 2
AVERAGE 70 μ M FLUX DENSITIES [mJy] AND ERRORS

S_{24} (mJy)	Redshift Range							
	0–0.4	0.4–0.6	0.6–0.8	0.8–1.0	1.0–1.2	1.2–1.6	1.6–2	2–3
0.06–0.08	1.65±0.18	0.60±0.09	0.64±0.09	0.63±0.08	0.73±0.10	0.77±0.09	<0.18±0.06	<0.01±0.07
0.08–0.10	1.81±0.20	1.82±0.20	1.42±0.16	0.94±0.12	1.23±0.15	1.17±0.13	0.32±0.08	<0.19±0.08
0.10–0.15	2.49±0.26	2.37±0.25	1.36±0.15	1.23±0.13	1.41±0.15	1.33±0.14	0.45±0.07	0.43±0.07
0.15–0.20	2.13±0.23	3.21±0.34	2.26±0.24	2.23±0.23	1.88±0.20	1.79±0.20	1.00±0.13	0.85±0.12
0.20–0.50	4.85±0.49	4.91±0.50	4.13±0.42	2.95±0.30	3.21±0.33	3.12±0.32	1.29±0.15	1.48±0.17
0.50–1.00	11.42±1.15	11.49±1.16	8.30±0.85	6.41±0.66	6.06±0.65	3.45±0.41	4.66±0.51	4.17±0.47
1.00–3.00	24.35±2.44	19.39±1.97	17.80±1.82	9.40±1.00	15.93±1.68	5.68±0.68	10.01±1.11	6.28±0.72

TABLE 3
AVERAGE 160 μ M FLUX DENSITIES [mJy] AND ERRORS

S_{24} (mJy)	Redshift Range							
	0–0.4	0.4–0.6	0.6–0.8	0.8–1.0	1.0–1.2	1.2–1.6	1.6–2	2–3
0.06–0.08	6.19±0.68	2.99±0.43	3.03±0.37	2.42±0.33	1.93±0.29	4.94±0.53	<2.29±0.32	<1.87±0.30
0.08–0.10	5.09±0.61	5.01±0.61	4.02±0.50	4.60±0.53	4.23±0.50	4.15±0.49	1.88±0.36	<2.79±0.40
0.10–0.15	7.70±0.83	7.25±0.78	8.48±0.88	7.00±0.73	5.10±0.55	6.96±0.73	4.44±0.48	4.90±0.56
0.15–0.20	8.11±0.88	8.34±0.93	8.92±0.95	6.28±0.69	9.92±1.05	10.22±1.07	6.20±0.69	6.10±0.72
0.20–0.50	15.07±1.52	15.62±1.60	15.16±1.54	12.74±1.30	11.47±1.18	17.50±1.79	6.95±0.73	9.92±1.05
0.50–1.00	28.72±2.91	27.14±2.78	30.95±3.17	24.62±2.55	19.85±2.19	17.57±2.03	18.88±2.09	17.19±1.89
1.00–3.00	51.58±5.21	51.28±5.30	39.69±4.13	26.11±3.01	32.53±3.97	<16.16±2.07	18.94±2.48	21.76±2.71

TABLE 4
AVERAGE $L_{\text{IR}} = L(8 - 1000\mu\text{M})$ IN [LOG L_{\odot}]

S_{24} (mJy)	Redshift Range							
	0–0.4 (0.3)	0.4–0.6 (0.5)	0.6–0.8 (0.7)	0.8–1.0 (0.9)	1.0–1.2 (1.1)	1.2–1.6 (1.4)	1.6–2 (1.8)	2–3 (2.3)
0.06–0.08	9.96±0.07	10.41±0.09	10.74±0.10	10.90±0.09	11.12±0.09	11.66±0.09	<11.60±0.10	<11.84±0.12
0.08–0.10	9.97±0.07	10.66±0.08	10.89±0.07	11.10±0.12	11.39±0.09	11.69±0.11	11.62±0.12	<12.01±0.14
0.10–0.15	10.16±0.06	10.82±0.07	11.11±0.10	11.27±0.12	11.47±0.10	11.84±0.09	11.88±0.13	12.22±0.18
0.15–0.20	10.18±0.07	10.89±0.08	11.19±0.08	11.35±0.08	11.69±0.10	12.00±0.08	12.06±0.11	12.36±0.20
0.20–0.50	10.49±0.07	11.16±0.08	11.46±0.10	11.61±0.10	11.82±0.11	12.24±0.17	12.12±0.20	12.55±0.22
0.50–1.00	10.81±0.07	11.44±0.06	11.77±0.10	11.92±0.10	12.07±0.11	12.33±0.19	12.55±0.15	12.83±0.20
1.00–3.00	11.10±0.07	11.69±0.07	11.95±0.07	11.98±0.09	12.34±0.08	12.23±0.11	12.68±0.20	13.04±0.23

NOTE. — Average redshifts and S_{24} for each bin are given in parentheses. Bins in which both 70 μ m and 160 μ m stacks resulted in non-detections are marked as upper limits.

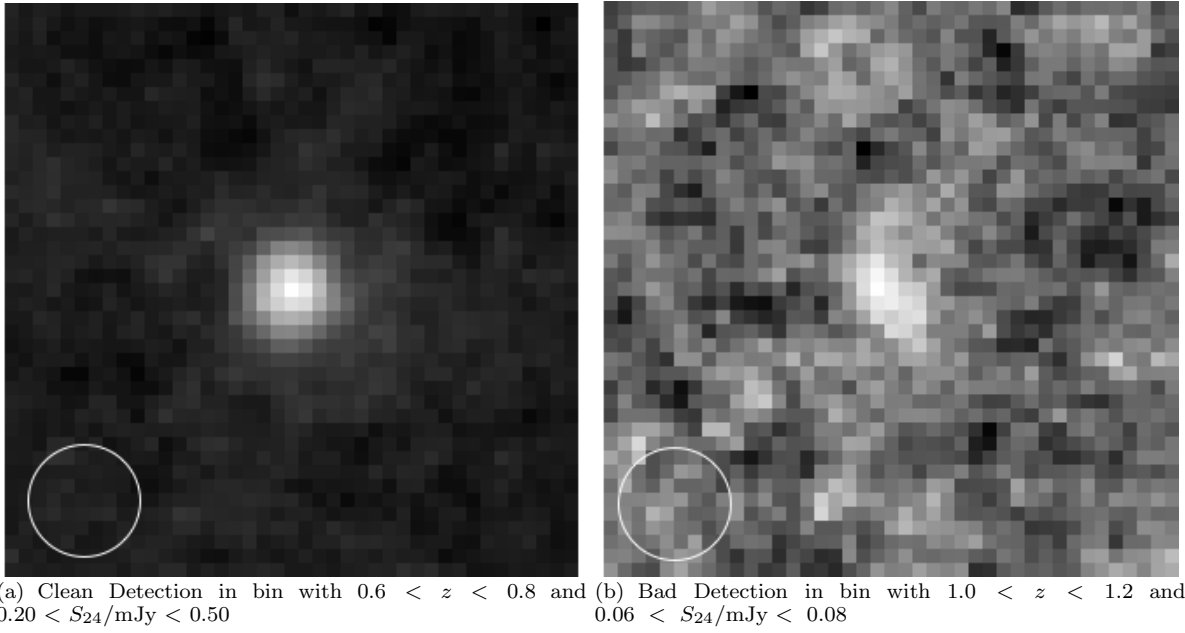


FIG. 1.— Examples of a clean detection at $70\ \mu\text{m}$ and a bad detection at $70\ \mu\text{m}$. The bad detection has a source in the center that does not resemble a clean point source, yet aperture photometry of this source yields a signal-to-noise of ~ 14 . The circles in the lower left hand corners are the size of the aperture used to measure our stacked fluxes.

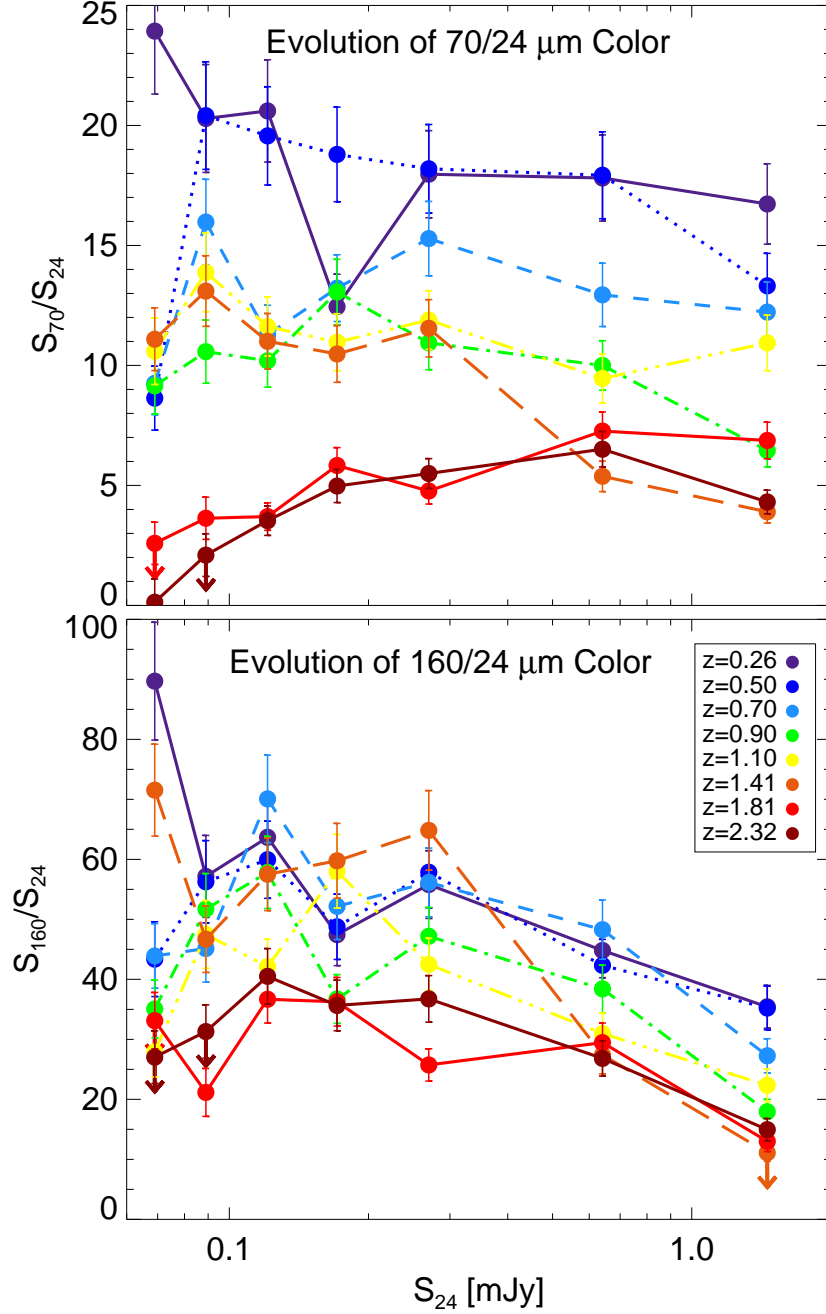


FIG. 2.— Stacked S_{70}/S_{24} (top) and S_{160}/S_{24} (bottom) flux ratios plotted as a function of S_{24} . Each color corresponds to a specific redshift bin, with bluer colors for low redshift and redder colors for high redshift bins. “Non-detections” are marked as upper limits, and 1σ error bars are plotted for the rest of the bins.

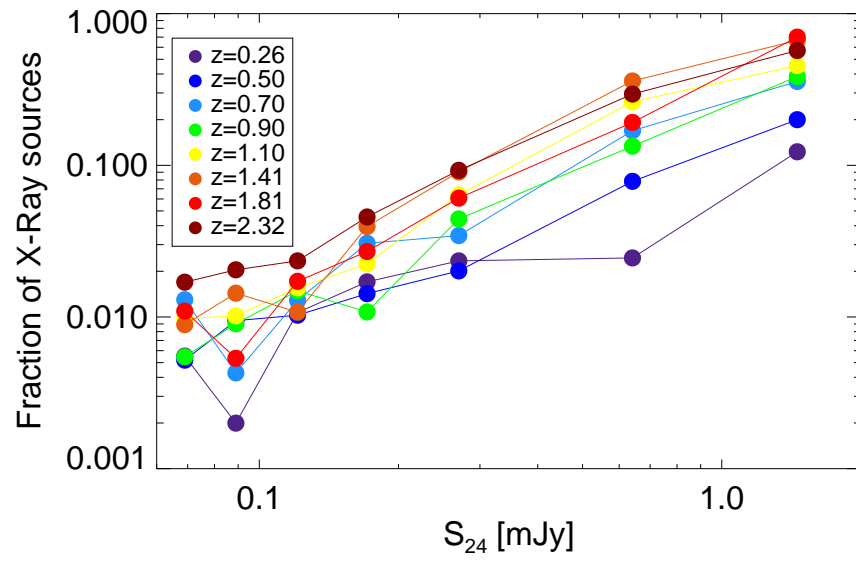


FIG. 3.— Fraction of sources in each bin that are also detected in the X-ray by *XMM-Newton*. At low S_{24} bins, X-ray sources account for a very small fraction of our sources, but at high flux and high redshift bins the X-ray sources begin to account for a large fraction of sources.

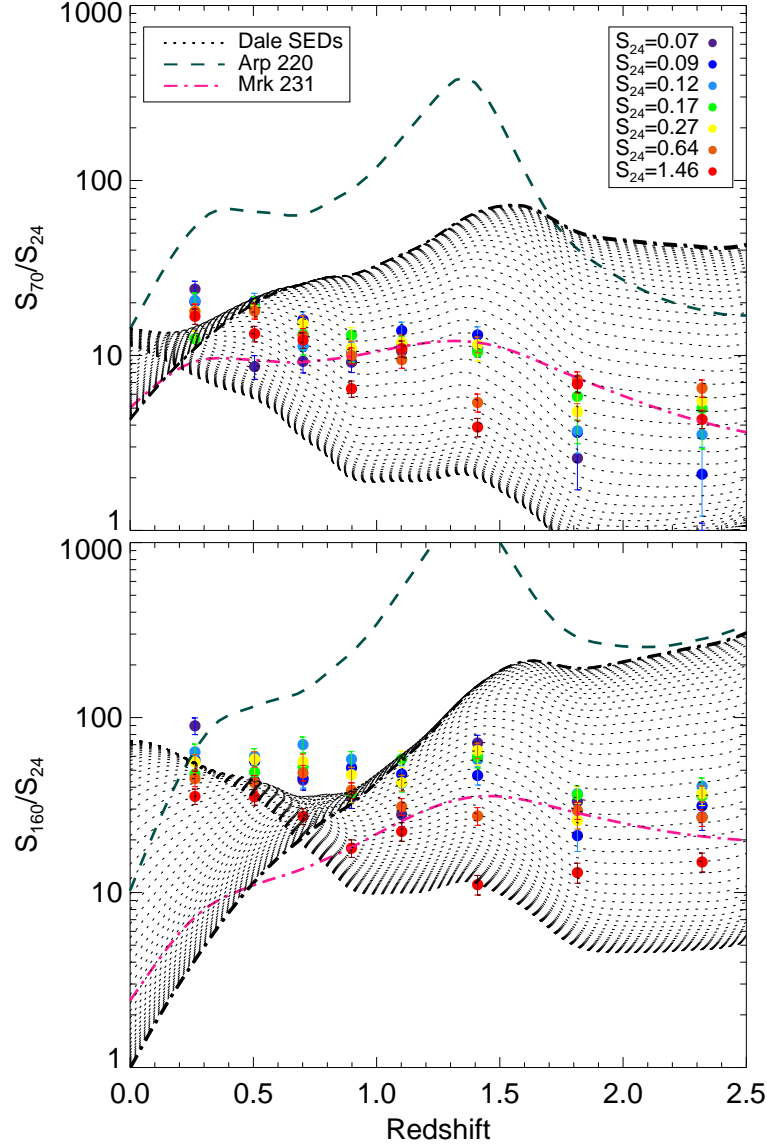


FIG. 4.— Stacked S_{70}/S_{24} and S_{160}/S_{24} flux ratios compared to models of “normal” star-forming galaxies from DALE (black lines; note: other empirical models cover a similar range) and models of Arp 220 (dark green line) and Mrk 231 (pink line) from SWIRE. The DALE models are a one parameter family of models, and we use the full range of DALE models, spanning $1 < \alpha < 2.5$. The model with the lowest α , and also the lowest L_{IR} , is designated by the dot-dashed line. Each colored dot represents a different S_{24} bin, with dimmer sources at the blue end of the spectrum and brighter sources represented by redder colors. We see that our stacked colors are consistent with those of the DALE galaxies and Mrk 231, but not with Arp 220.

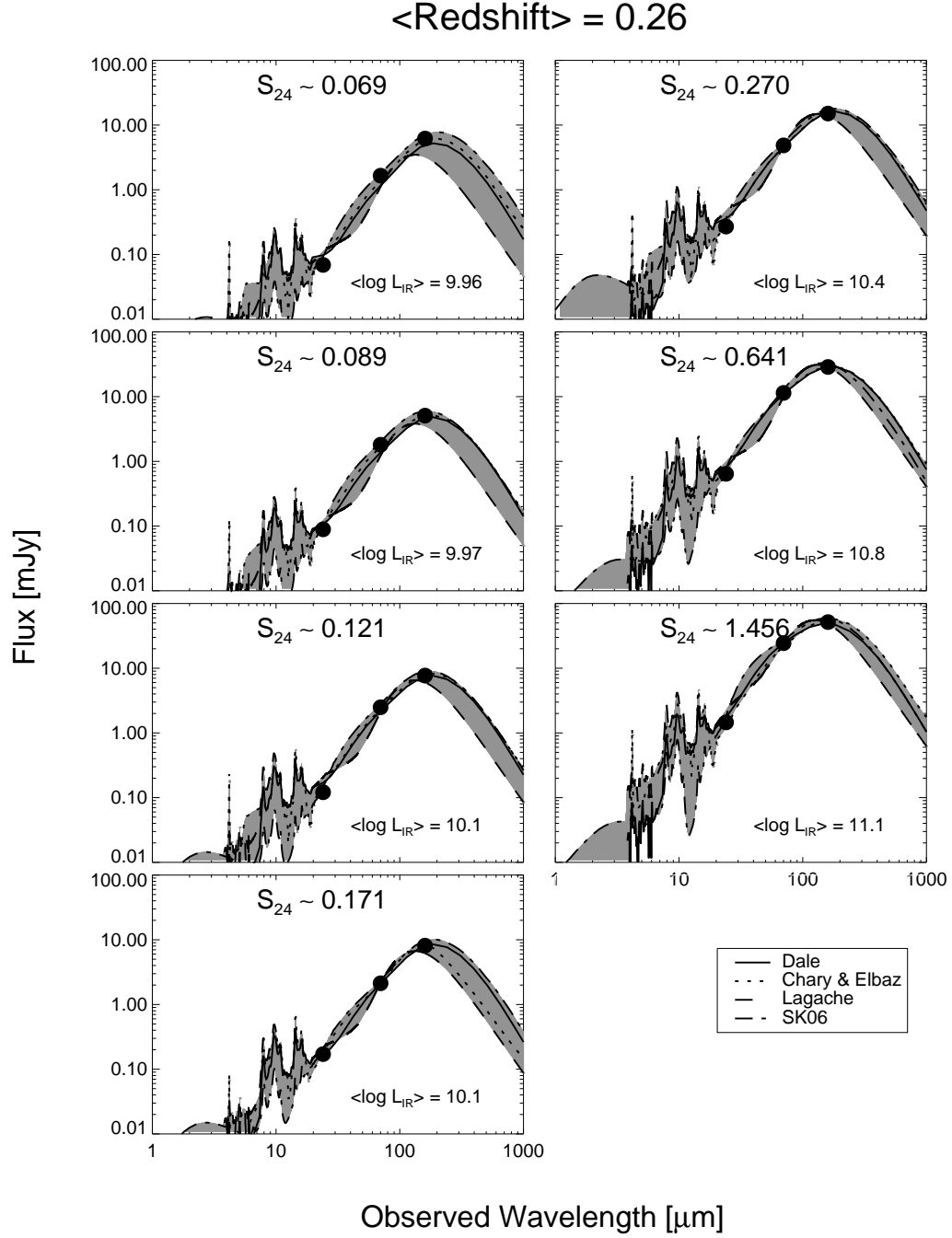


FIG. 5A.— SED fits to stacked fluxes in each S_{24} bin at a redshift $0 \leq z \leq 0.4$. The region spanned by the best-fit SEDs from each library is shaded. Non-detections are marked as upper limits, and the errors on the rest of the points are smaller than the size of the dot. Libraries used are from Dale & Helou (solid line), Chary & Elbaz (dotted line), Lagache et al. (dashed line), and Siebenmorgen & Krügel (dot-dashed line). Figures 5b–5h are available in the online version of the Journal.

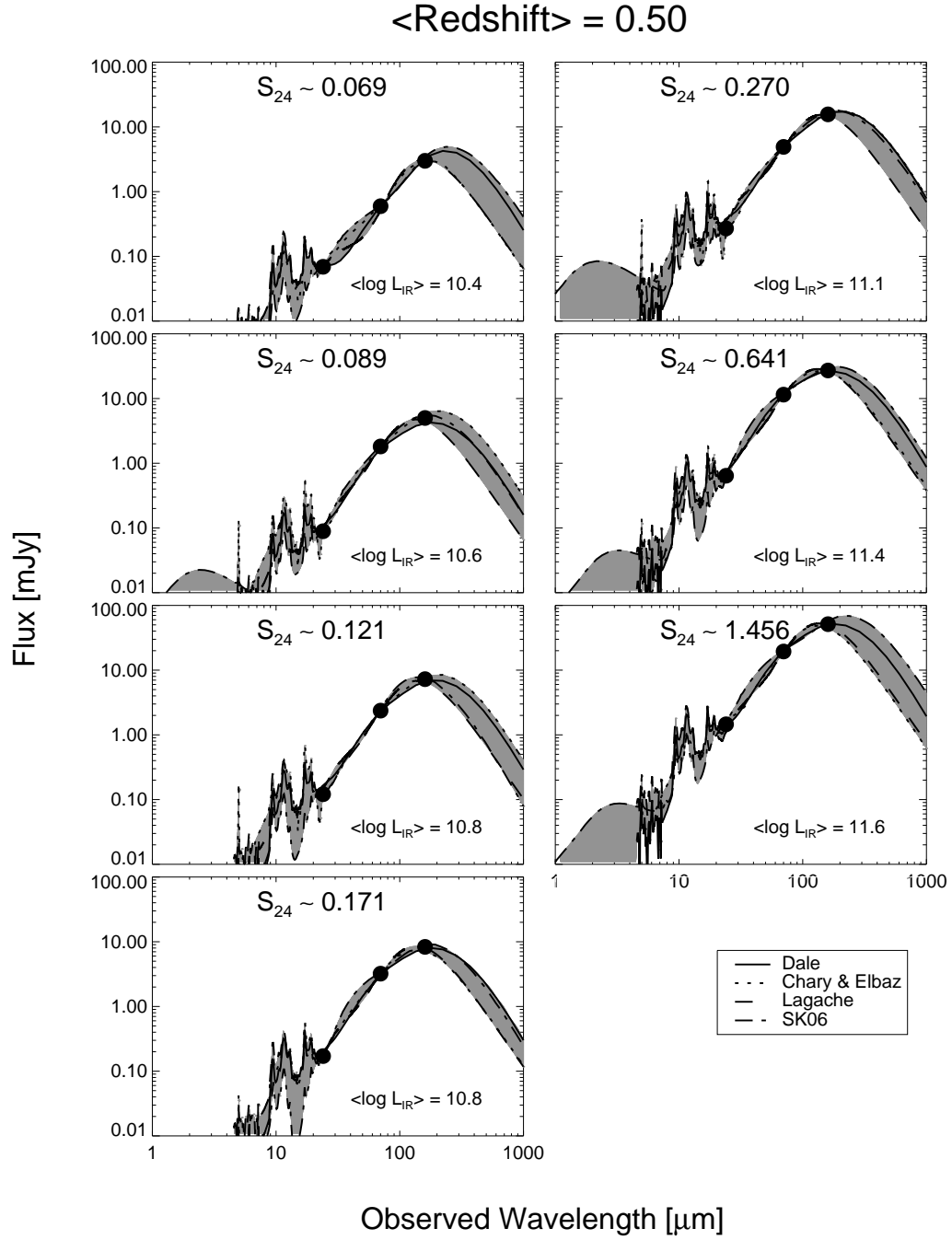


FIG. 5B.— SED fits to stacked fluxes in each S_{24} bin at a redshift $0.4 \leq z \leq 0.6$. The region spanned by the best-fit SEDs from each library is shaded. Non-detections are marked as upper limits, and the errors on the rest of the points are smaller than the size of the dot. Libraries used are from Dale & Helou (solid line), Chary & Elbaz (dotted line), Lagache et al. (dashed line), and Siebenmorgen & Krügel (dot-dashed line).

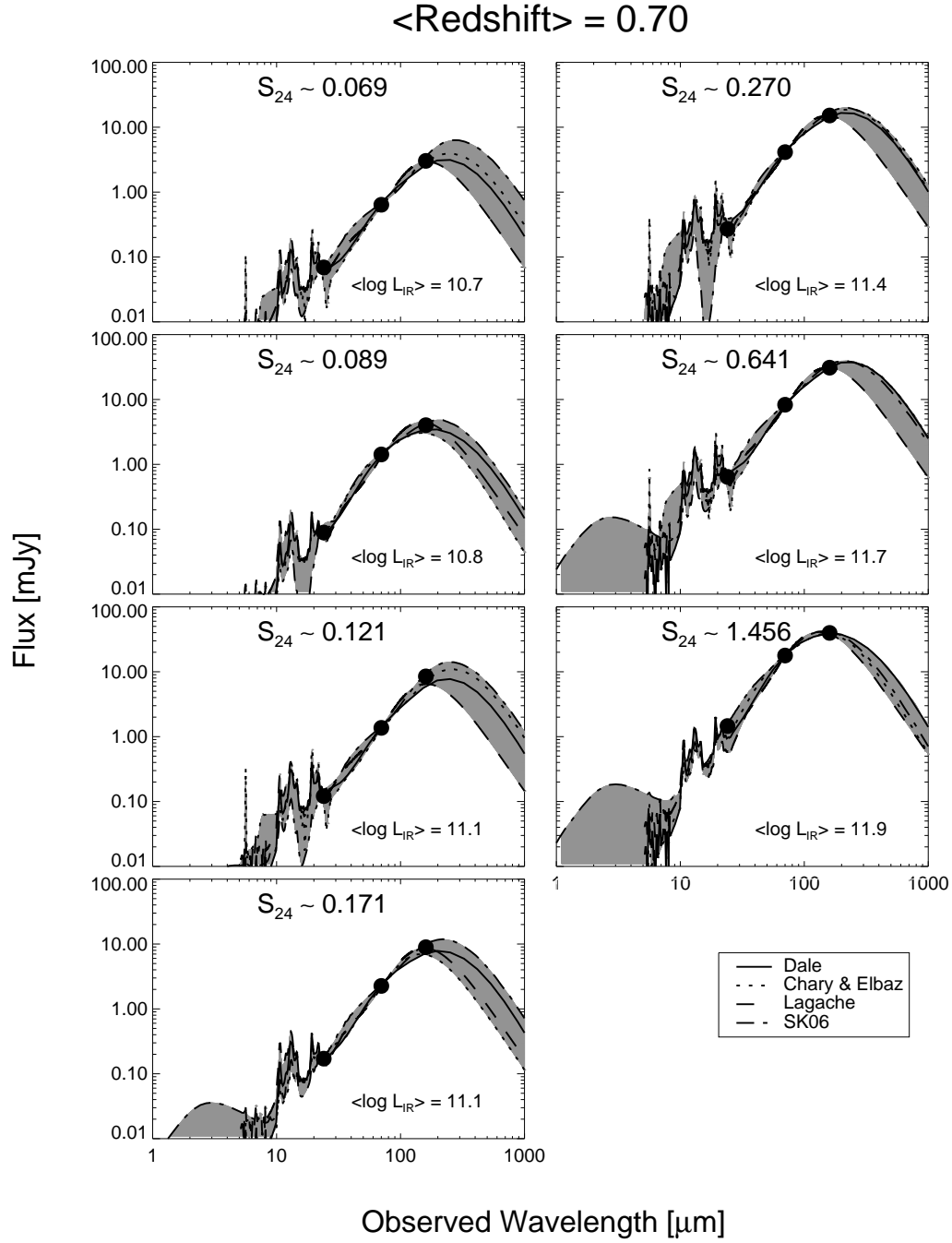


FIG. 5C.— SED fits to stacked fluxes in each S_{24} bin at a redshift $0.6 \leq z \leq 0.8$. The region spanned by the best-fit SEDs from each library is shaded. Non-detections are marked as upper limits, and the errors on the rest of the points are smaller than the size of the dot. Libraries used are from Dale & Helou (solid line), Chary & Elbaz (dotted line), Lagache et al. (dashed line), and Siebenmorgen & Krügel (dot-dashed line).

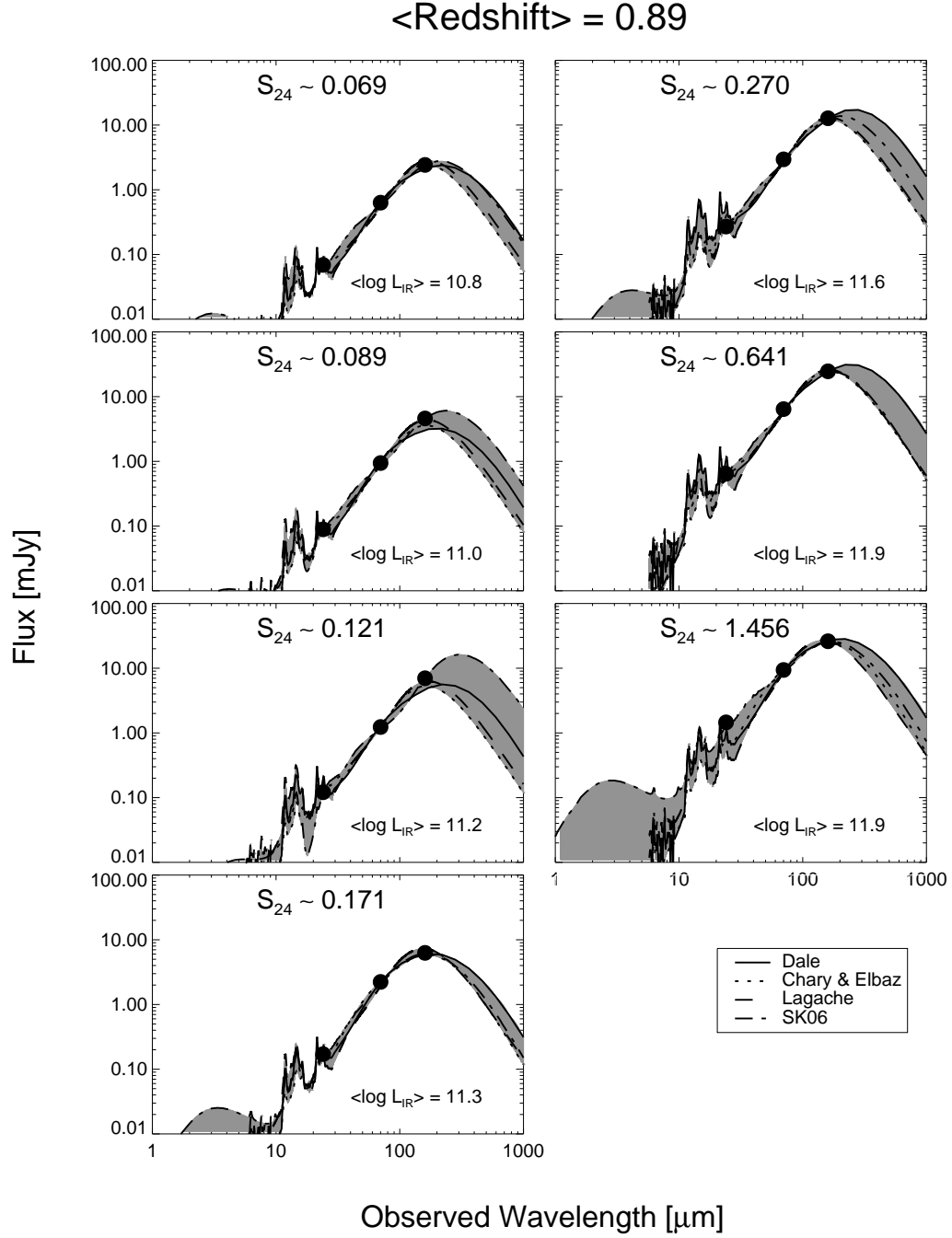


FIG. 5D.— SED fits to stacked fluxes in each S_{24} bin at a redshift $0.8 \leq z \leq 1.0$. The region spanned by the best-fit SEDs from each library is shaded. Non-detections are marked as upper limits, and the errors on the rest of the points are smaller than the size of the dot. Libraries used are from Dale & Helou (solid line), Chary & Elbaz (dotted line), Lagache et al. (dashed line), and Siebenmorgen & Krügel (dot-dashed line).

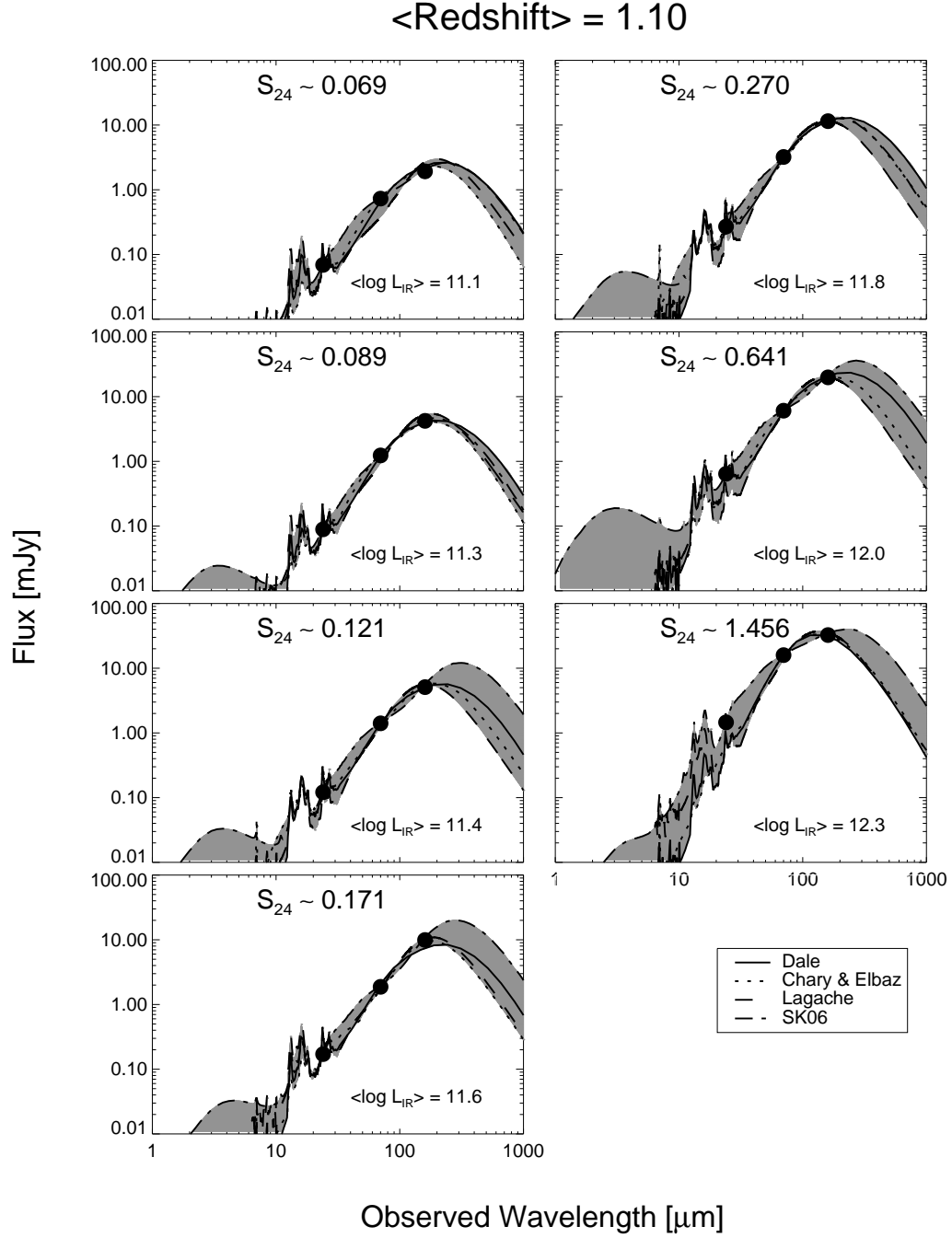


FIG. 5E.— SED fits to stacked fluxes in each S_{24} bin at a redshift $1.0 \leq z \leq 1.2$. The region spanned by the best-fit SEDs from each library is shaded. Non-detections are marked as upper limits, and the errors on the rest of the points are smaller than the size of the dot. Libraries used are from Dale & Helou (solid line), Chary & Elbaz (dotted line), Lagache et al. (dashed line), and Siebenmorgen & Krügel (dot-dashed line).

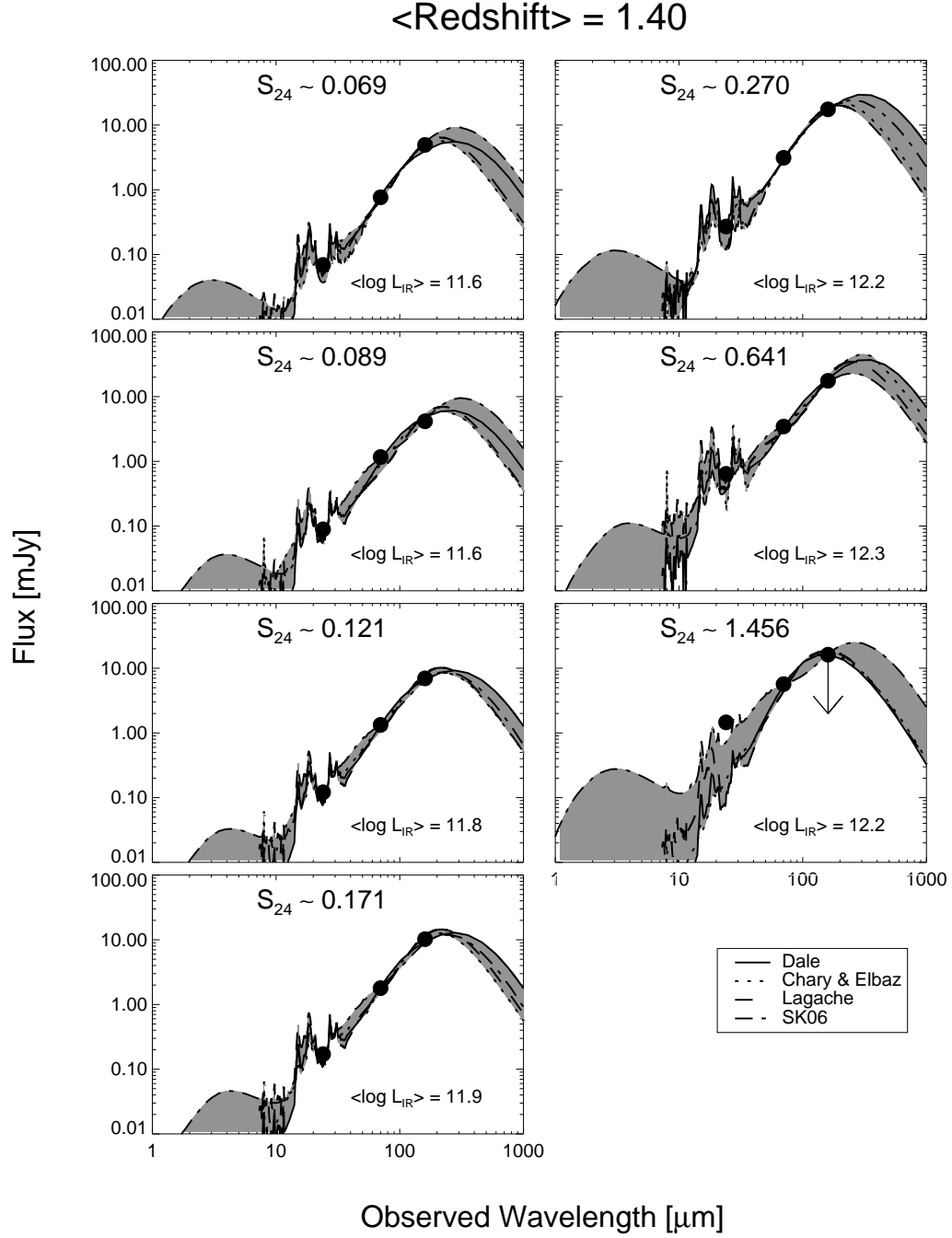


FIG. 5F.— SED fits to stacked fluxes in each S_{24} bin at a redshift $1.2 \leq z \leq 1.6$. The region spanned by the best-fit SEDs from each library is shaded. Non-detections are marked as upper limits, and the errors on the rest of the points are smaller than the size of the dot. Libraries used are from Dale & Helou (solid line), Chary & Elbaz (dotted line), Lagache et al. (dashed line), and Siebenmorgen & Krügel (dot-dashed line).

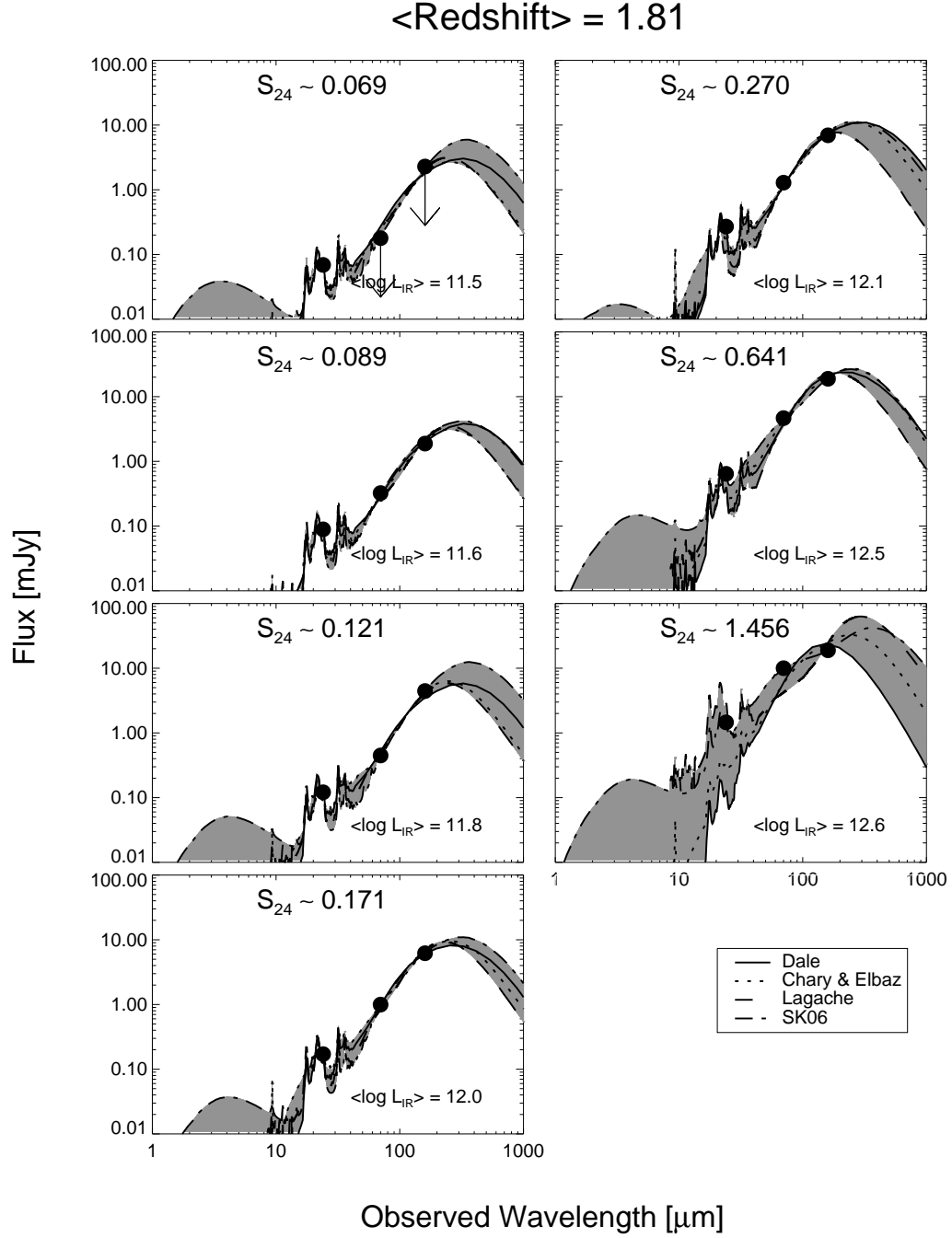


FIG. 5G.— SED fits to stacked fluxes in each S_{24} bin at a redshift $1.6 \leq z \leq 2.0$. The region spanned by the best-fit SEDs from each library is shaded. Non-detections are marked as upper limits, and the errors on the rest of the points are smaller than the size of the dot. Libraries used are from Dale & Helou (solid line), Chary & Elbaz (dotted line), Lagache et al. (dashed line), and Siebenmorgen & Krügel (dot-dashed line).

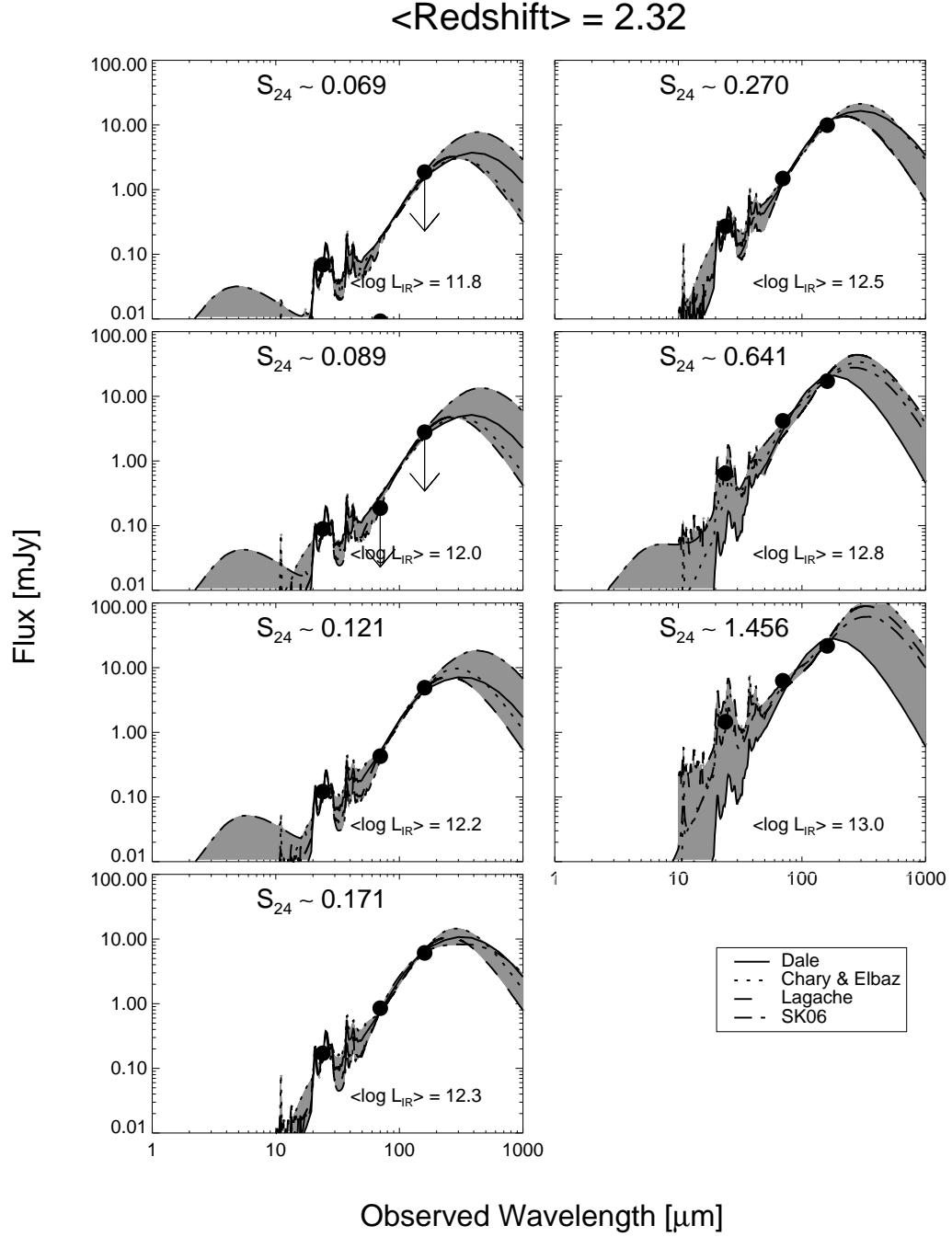


FIG. 5H.— SED fits to stacked fluxes in each S_{24} bin at a redshift $2.0 \leq z \leq 3.0$. The region spanned by the best-fit SEDs from each library is shaded. Non-detections are marked as upper limits, and the errors on the rest of the points are smaller than the size of the dot. Libraries used are from Dale & Helou (solid line), Chary & Elbaz (dotted line), Lagache et al. (dashed line), and Siebenmorgen & Krügel (dot-dashed line).

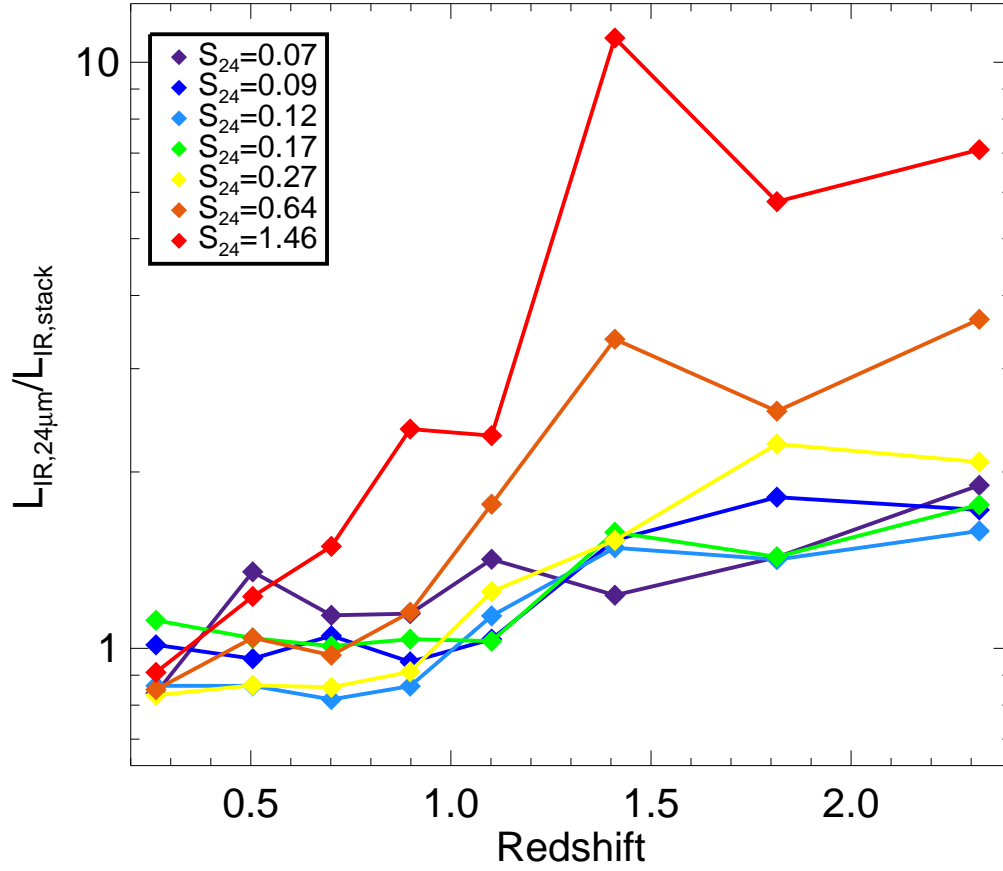


FIG. 6.— Ratio of L_{IR} derived from only using S_{24} vs. L_{IR} derived from our stacking analysis. There is fairly good agreement between the two methods at low redshifts, but at higher redshifts we see that previous methods using only $24\mu\text{m}$ flux overestimate the true luminosity, especially in the brighter $24\mu\text{m}$ flux bins.

REFERENCES

- Bertin, E., & Arnouts, S. 1996, *A&AS*, 117, 393
- Blain, A. W., Smail, I., Ivison, R. J., Kneib, J., & Frayer, D. T. 2002, *Phys. Rep.*, 369, 111
- Brusa, M., et al. 2010, *ArXiv e-prints*
- Calzetti, D., et al. 2007, *ApJ*, 666, 870
- Chary, R., & Elbaz, D. 2001, *ApJ*, 556, 562
- Dale, D. A., & Helou, G. 2002, *ApJ*, 576, 159
- Dole, H., et al. 2006, *A&A*, 451, 417
- Dye, S., Eales, S. A., Ashby, M. L. N., Huang, J., Egami, E., Brodwin, M., Lilly, S., & Webb, T. 2007, *MNRAS*, 375, 725
- Frayer, D. T., et al. 2009, *AJ*, 138, 1261
- Gordon, K. D., et al. 2007, *PASP*, 119, 1019
- Houck, J. R., et al. 2005, *ApJ*, 622, L105
- Ilbert, O., et al. 2009, *ApJ*, 690, 1236
- Lagache, G., Dole, H., & Puget, J. 2003, *MNRAS*, 338, 555
- Lagache, G., et al. 2004, *ApJS*, 154, 112
- Laurent, O., Mirabel, I. F., Charmandaris, V., Gallais, P., Madden, S. C., Sauvage, M., Vigroux, L., & Cesarsky, C. 2000, *A&A*, 359, 887
- Le Floc'h, E., et al. 2005, *ApJ*, 632, 169
- . 2009, *ApJ*, 703, 222
- Lilly, S. J., et al. 2007, *ApJS*, 172, 70
- McCracken, H. J., et al. 2010, *ApJ*, 708, 202
- Papovich, C., et al. 2007, *ApJ*, 668, 45
- Polletta, M., et al. 2007, *ApJ*, 663, 81
- Rieke, G. H., et al. 2004, *ApJS*, 154, 25
- Salvato, M., et al. 2009, *ApJ*, 690, 1250
- Sanders, D. B., & Mirabel, I. F. 1996, *ARA&A*, 34, 749
- Sanders, D. B., et al. 2007, *ApJS*, 172, 86
- Scoville, N., et al. 2007, *ApJS*, 172, 1
- Siebenmorgen, R., & Krügel, E. 2007, *A&A*, 461, 445
- Stansberry, J. A., et al. 2007, *PASP*, 119, 1038
- Stetson, P. B. 1987, *PASP*, 99, 191
- White, R. L., Helfand, D. J., Becker, R. H., Glikman, E., & de Vries, W. 2007, *ApJ*, 654, 99
- Zheng, X. Z., Bell, E. F., Rix, H., Papovich, C., Le Floc'h, E., Rieke, G. H., & Pérez-González, P. G. 2006, *ApJ*, 640, 784